



Structural, electrical, and leakage current characteristics of Sr(Sn,Se)O₃ modified Bi_{0.5}Na_{0.5}TiO₃ ferroelectric ceramics

B. B. Arya^{1,a)}, R. N. P. Choudhary¹

¹Department of Physics, Siksha 'O' Anusandhan (Deemed to Be University), Bhubaneswar, Odisha, India

^{a)}Address all correspondence to this author. e-mail: bbarya96@gmail.com

Received: 14 March 2023; accepted: 19 June 2023; published online: 10 July 2023

This paper reports the synthesis and detailed discussion of structural, electrical and leakage current characteristics of strontium stannate-selenite (Sr(Sn,Se)O₃) modified bismuth sodium titanate (Bi_{0.5}Na_{0.5}TiO₃) compounds with standard formula (1–2x) (Bi_{0.5}Na_{0.5})TiO₃ + x(SrSnO₃) + x(SrSeO₃) with x = 0, 0.05, 0.10, 0.15. The materials have been fabricated through a mixed oxide reaction route. The room temperature X-ray structural analysis indicates the formation of single-phase compounds with a rhombohedral crystal system. The SEM micrograph suggests the even distributions of grains with a very small number of voids. Detailed studies of frequency (1 kHz to 1 MHz) and temperature (25–500 °C) dependence of dielectric and other electrical parameters of the studied compounds were obtained using the programmable LCR meter. The ferroelectric behavior in the compounds is confirmed by the P–E hysteresis loop. The J–E characteristics of the materials have shown a very small amount of leakage current density with the presence of an Ohmic conduction mechanism.

Introduction

Lead-based piezoelectric ceramics are extensively used for different electronic device applications, like transducers, sensors, actuators, micro-electromechanical systems (MEMS), and various memories [1, 2]. Among them, lead zirconate titanate Pb(Zr_{1-x}Ti_x)O₃ (PZT) and the related compounds have drawn the special attention of researchers because of their excellent piezoelectric as well as their non-linear electro-optic properties. Some PZT-based compounds have essential applications in the field of actuators, sensors, electrical resonators, speakers, underwater communications, wave filters, transducers, hydrophones, etc. [3]. PZT exhibits a perovskite structure and becomes non-centrosymmetric below the Curie point (i.e., T_c = 350 °C). It demonstrates the highest piezoelectric property and the highest permittivity near the MPB (morphotropic phase boundary) which separates the region with both rhombohedral as well as tetragonal phases with Zr:Ti of 52:48 [4]. However, PZT has some disadvantages including evaporation of toxic lead during the synthesis process causing serious environmental pollution and health hazard, and fatigue while cycled more than 10⁷ times. These shortcomings of PZT reduce

its enormous applications in various fields. Recently, some lead-free piezoelectric ceramic compounds have drawn more attention from researchers for different electronic applications with their comparable characteristics same as PZT. Among the lead-free piezoelectric ceramics, bismuth sodium titanate (Bi_{0.5}Na_{0.5}TiO₃) (abbreviated as BNT) has been taken as the most promising candidate for device applications because of its excellent ferroelectric and related properties. This material (BNT) was first discovered in 1960 by Smolenskii et al. [5]. At room temperature, it possesses a perovskite-type configuration with a rhombohedral crystal structure. It also exhibits a phase transition from the rhombohedral phase (ferroelectric) to the tetragonal phase (anti-ferroelectric) at around 300 °C (called depolarization temperature (T_d)) and from the tetragonal phase (anti-ferroelectric) to the cubic phase (paraelectric) at about 540 °C [6]. It is a strong ferroelectric material with large value of remnant polarization (i.e., P_r = 38 μC/cm²) and relatively high Curie point (i.e., T_c = 320 °C) [7]. The single crystal of BNT shows a dielectric peak at around 320 °C. In recent times, the structural phase transformation of the single crystal of BNT has been studied by using the powder neutron diffraction data

[8] and revealed the structural change from the rhombohedral phase (space group, R3c) to the tetragonal phase (space group, P4bm). Recently, an important development has taken place to achieve the energy storing property in the BNT-based thin film. The increased energy storage of BNT films occurs due to its large value of dielectric constant along with the polarization of the material [9]. As reported by Zhai et al. [10], BNT-BKT-ST thin film, where bismuth potassium titanate is BKT and strontium titanate is ST, has a high energy-storage density (20 J/cm^3) together with moderate energy-storage efficiency (i.e., 65.17%). Nevertheless, the high value of conductivity and the large coercive field (i.e., $E_c = 7.30 \text{ kV/mm}$) of the BNT system creates problems in its poling process. Therefore, BNT ceramic displays a relatively small piezoelectric coefficient ($d_{33} = 58 \text{ pC/N}$) as compared to that of PZT [11]. This is the major disadvantage of this compound which confines its applications. Hence, in order to solve the problem and enhance the physical properties, a solid solution of BNT with other compounds of similar/dissimilar structures is made. The alkaline earth stannates with perovskite structure of a general formula MSnO_3 (with $M = \text{Ba, Ca, Sr}$) have drawn significant attention as dielectric ceramic. These compounds have extensively been used (as industrial and technical compounds) for the manufacturing of chemical sensors [12], thermally capable capacitors [13], water photo-electrolysis systems [14], humidity sensors [15], gas sensors, semiconductor sensors, flat panel displays [16], antistatic coatings [17], and Li-ion battery [18]. Alkaline earth stannates are also used as transparent conducting oxides for the development of transparent electrodes in the field of photovoltaic cells as well as organic LED. SrSnO_3 (abbreviated as SSn) is recognized as a wide band gap (4–5 eV) semiconductor with low effective mass [19]. It has the orthorhombic crystal system (space group, Pbnm) with a direct gap or two band gaps closely related to energy [20]. The cell constants of the SSn perovskite are; $a = 5.717 \text{ \AA}$, $b = 5.729 \text{ \AA}$, $c = 8.084 \text{ \AA}$ [21]. Like SSn, other compounds of the family also exhibit attractive dielectric and other properties because of their high efficiency as well as easy synthesis. Another group of perovskite, i.e., alkaline earth selenites with a common formula XSeO_3 ($X = \text{Ba, Ca, Sr}$) have also drawn great attention from researchers in recent times due to their attractive ferroelectric properties. The metal selenites which possess transition metals with d^0 electronic configuration have widely been taken for research because of their potential applications in the field of photoelectric materials, like pyroelectric, second-order NLO (nonlinear optical) compounds, and piezoelectric ceramics [22]. The selenium compounds having 4+ oxidation states comprise versatile applications according to their practical as well as scientific value. These compounds are used in the fields of agriculture, electronic industries, organic synthesis, glass industries, chemical laboratories, medicine, etc. [23]. SrSeO_3 exhibits monoclinic centro-symmetric structure

(space group, $P2_1/m$) with the unit cell dimension; $a = 4.456(1) \text{ \AA}$, $b = 5.478(1) \text{ \AA}$, $c = 6.574(1) \text{ \AA}$, $\beta = 107.34 (1)^\circ$, cell volume (V) = $153.2(1) \text{ \AA}^3$, (where the number in parenthesis represents the standard deviation), calculated density (ρ_{cal}) = 4.65 g/cm^3 and coordination number $Z = 2$. In this compound, Sr^{2+} cations are of nine fold coordination with the average bond length of $\text{Sr-O} = 2.741 \text{ \AA}$. [24]. Selenite glasses are considered as a new and an exotic type of non-traditional glass. In the glass composition, with the rise in the SeO_2 percentage, the coordination number of Se changes from 4 to 3 which causes the transformation of the oxygen-rich selenate phase to the oxygen-deficient selenite phase, and as a result, the optical and electrical properties along with the network structure of the glass are affected [25]. The SeO_2 -containing glass possesses high ionic conductivity at room temperature (i.e., 10^{-3} – 10^{-4} S/cm) because of the high value of polarizability of the selenium ion [26]. The complex composition of SeO_2 glasses acts as the potential candidate for technical applications including super ionic semiconductors, nonlinear optical devices, reflecting windows, sensors, soluble micro-fertilizers, infrared transmission components, etc. The major benefit of introducing SeO_2 to glass composition is its capability of decreasing the melting point of the compositions and modifying the optical properties [27]. Taking into consideration the above significant results of SrSnO_3 as well as SrSeO_3 , it is proposed to synthesize the composition of BNT with these two compounds with the standard formula $(1-2x)(\text{Bi}_{0.5}\text{Na}_{0.5})\text{TiO}_3 + x(\text{SrSnO}_3) + x(\text{SrSeO}_3)$ for their detailed studies of dielectric, electrical, ferroelectric, and leakage current characteristics. It has been found that the above properties of the BNT ceramic have significantly modified on the addition of an equal amount of SSn+SSe to it.

Results and discussions

Structural analysis

Figure 1(a) represents the room temperature X-ray diffraction pattern of the calcined powder of the BNT+SSn+SSe with various concentrations. X-ray diffraction is a widely used technique for structural analysis and phase identification of powder samples. The above XRD pattern with the sharp as well as clear peaks suggests the crystallization of the materials in a single-phase perovskite structure without any extra (impurity) peak. The characteristic peaks of the prepared materials ranging from 20° to 80° (in 2θ scale) are completely different from those of the constituent ones (ingredients) determining the formation of new perovskite compounds. The structure of materials in rhombohedral symmetry was analyzed by taking the unit cell parameters; $a = 5.4760 \text{ \AA}$ and $c = 6.7780 \text{ \AA}$ of sodium bismuth titanium oxide and all the peaks were indexed by using the X'Pert Highscore software (reference code ICDD-00-036-0340) [28].

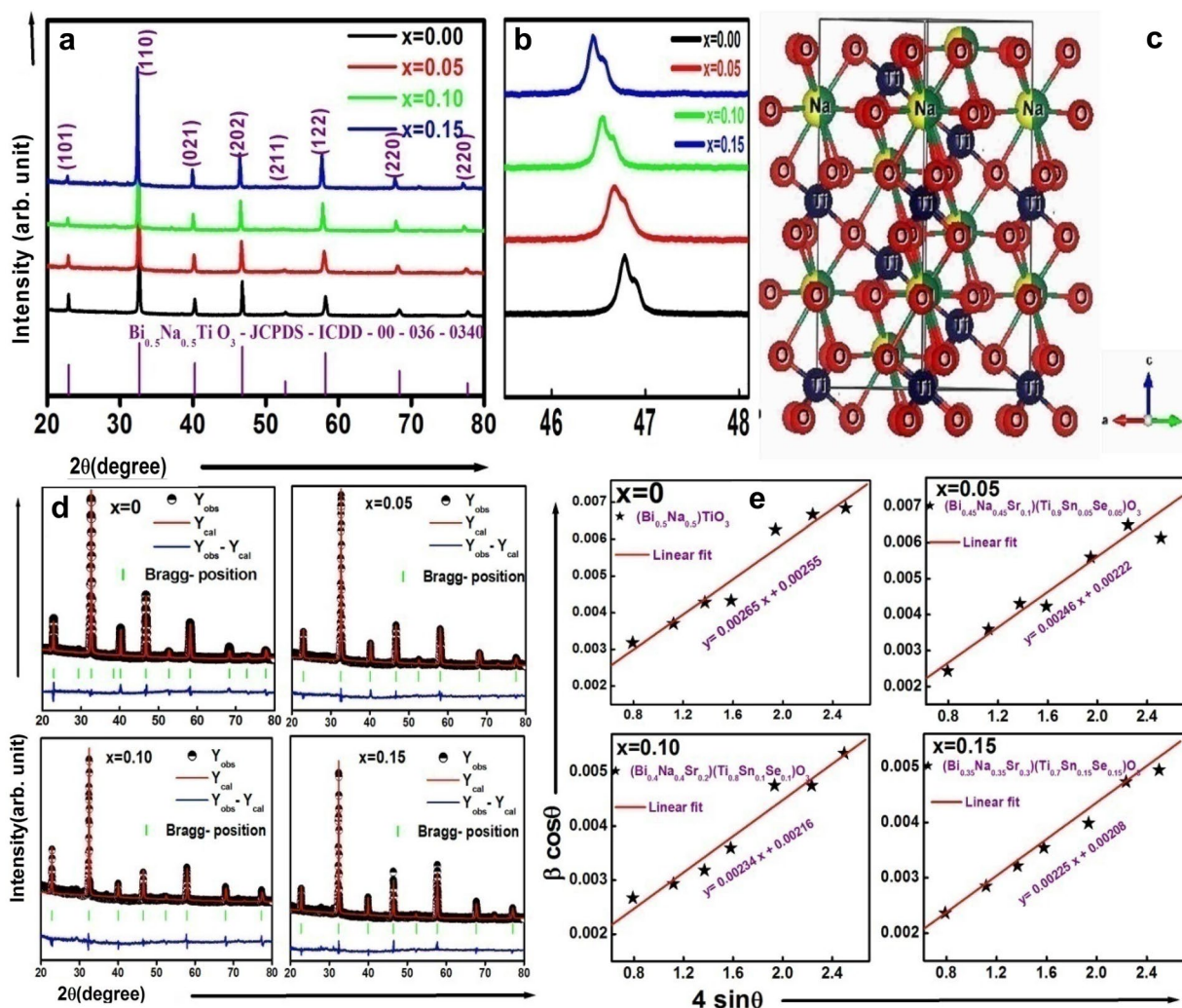


Figure 1: (a) Room temperature XRD spectrum; (b) Shifting of XRD peaks of $(1-2x)$ BNT + x SSn + x SSe compounds with various concentrations; (c) Rhombohedral structure of $(\text{Bi}_{0.5}\text{Na}_{0.5})\text{TiO}_3$; (d) Rietveld Refinement; and (e) Williamson-Hall plot of $(1-2x)$ BNT + x SSn + x SSe compounds with various concentrations.

It is visible that with the increase in the amount of the substituted materials (SSn+SSe) in BNT, the peaks of the XRD pattern move toward the lower side of 2θ (shown in Fig. 1b). It is because of the ionic radius of the BNT compound is smaller than that of the other substituted compounds.

Figure 1(c) represents the schematic diagram of the pure $(\text{Bi}_{0.5}\text{Na}_{0.5})\text{TiO}_3$ sample in a ball-stick arrangement. Here, the corresponding elements are designed in different colors and labeled by their names. The rhombohedral structure of the bismuth sodium titanate possesses the cell parameters which are comparable with those of obtained results.

For detailed structural analysis of the prepared materials, the Rietveld refinement method was performed using Maud software. The XRD spectra of the compounds are compared with that of a replicated model achieved from the CIF file (CIF: NIMS_Mat-Navi_4295277669_1_2) of $(\text{Bi}_{0.5}\text{Na}_{0.5})\text{TiO}_3$ compound

having rhombohedral crystal system with space group, $R3c$. The refined cell parameters of the parent and modified compounds are comparable with those of the reported one [29]. In Fig. 1(d), the black solid symbols are the experimental data/pattern, the red line represents Rietveld refinement simulation, and the blue line signifies the difference between the experimental data and simulation, and the green solid symbol represents the corresponding Bragg's position of the diffraction peaks. It is clear that, the Rietveld refinements provide reasonable simulation to the data with the goodness of fit (σ) values provided in Table 1. The refined unit cell dimension and the reliability parameters (i.e., R_{wp} , R_b , R_{exp}) of all the prepared compounds are compared in Table 1. The detailed information regarding the reliability index/parameters is well explained in the previous communication [30].

To determine the crystalline sizes of the of the studied materials and further confirm its strains, the Williamson-Hall equation

was utilized, simply expressed as by the following equation [31, 32],

$$\beta_{hkl} \cos \theta = \frac{k\lambda}{D} + 4\epsilon \sin \theta \quad (1)$$

where β_{hkl} is the full width at half maximum (FWHM) value for each diffraction peak, K is the shape factor (0.94 for rhombohedral system), λ is the wavelength of $\text{CuK}\alpha$ (0.15406 nm) radiation, D represents the crystalline size, and ϵ is the integral breadth related to the strain. Hence, by plotting the graph of $\beta_{hkl} \cos \theta$ against $4\sin \theta$, the crystalline size and the lattice strain of samples can be estimated from the intercept and slope of the Williamson–Hall plot, respectively as shown in Fig. 1e. The calculated values of crystallite size and the lattice strain are tabulated in Table 1.

Micro-structural analysis

Figure 2 depicts the surface morphology of the gold-sputtered sintered samples (BNT+SSn+SSe) for various concentrations. This figure exhibits that the primarily rectangular grains are densely packed with a few voids all over the surface. The well-defined grains are distributed uniformly and separated by the walls known as the grain boundary. The various shapes and sizes of the grains suggest the polycrystalline nature of the studied materials. For all four compositions of the materials, the size of the grains varies from 0.28 to 1.61 μm , and the average value of grain size is calculated to be 0.41 μm , 0.57 μm , 0.78 μm , 1.17 μm for $x=0, 0.05, 0.10, 0.15$ respectively. With the increase in the percentage of x , the average grain size of the studied material increases. From Table 1, the calculated values of crystallite size of each composition are less than that of grain sizes. It is noteworthy that this difference results from the fact that the grains are consisted of several crystallites, probably due to internal stresses and/or defects in the structure [33].

Dielectric study

The dielectric properties of the ceramic compounds depend on two features i.e., dielectric constant and loss tangent [34]. These two components play vital roles in the potential application of

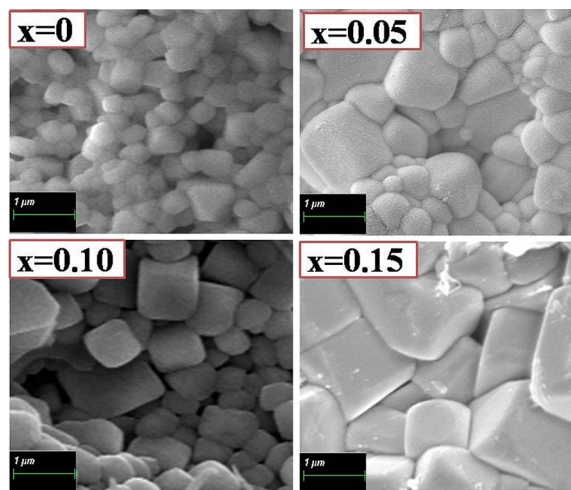


Figure 2: SEM micrographs of (1–2x) BNT+x SSn+x SSe compounds with various concentrations.

the dielectric materials. These two factors depend on the structure, chemical composition, and defects present in the materials along with the experimental condition like frequency and temperature. The dielectric constant determines the charge storing capacity of a material; whereas the loss tangent represents the ratio of the dissipation of energy and the storage of energy in a dielectric capacitor. The tangent loss ($\tan \delta$) can be expressed in the real (Z') as well as imaginary (Z'') parts of the impedance, and also in terms of ac conductivity (σ_{ac}) as follows,

$$\tan \delta = \frac{Z''}{Z'} \quad (2)$$

$$\text{and } \tan \delta = \frac{\sigma_{ac}}{\omega \epsilon_0 \epsilon_r} \quad (3)$$

where ω represents the angular frequency and ϵ_0 represents the permittivity in the vacuum.

Effect of frequency on dielectric parameters

Figure 3(a), (b) show the measured response of the applied ac signal on relative permittivity and tangent loss of the studied materials (BNT+SSn+SSe) for varying amounts of additives (0,

TABLE 1: Unit cell dimension, reliability parameters, crystallite size and lattice strain of (1–2x) BNT+x SSn+x SSe with various concentrations.

x	Crystal structure and space group	Lattice parameters (Å)		Reliability parameters (%)				Crystallite size (D) (nm)	Lattice strain
		a	c	R_{wp}	R_b	R_{exp}	gof		
0	Rhombohedral and $R3c$	5.490	13.499	10.80	10.27	5.43	1.99	57	0.0026
0.05		5.505	13.416	10.90	10.17	6.52	1.67	65	0.0024
0.10		5.529	13.534	11.28	10.28	6.67	1.69	67	0.0023
0.15		5.535	13.598	11.37	10.50	7.24	1.57	70	0.0022

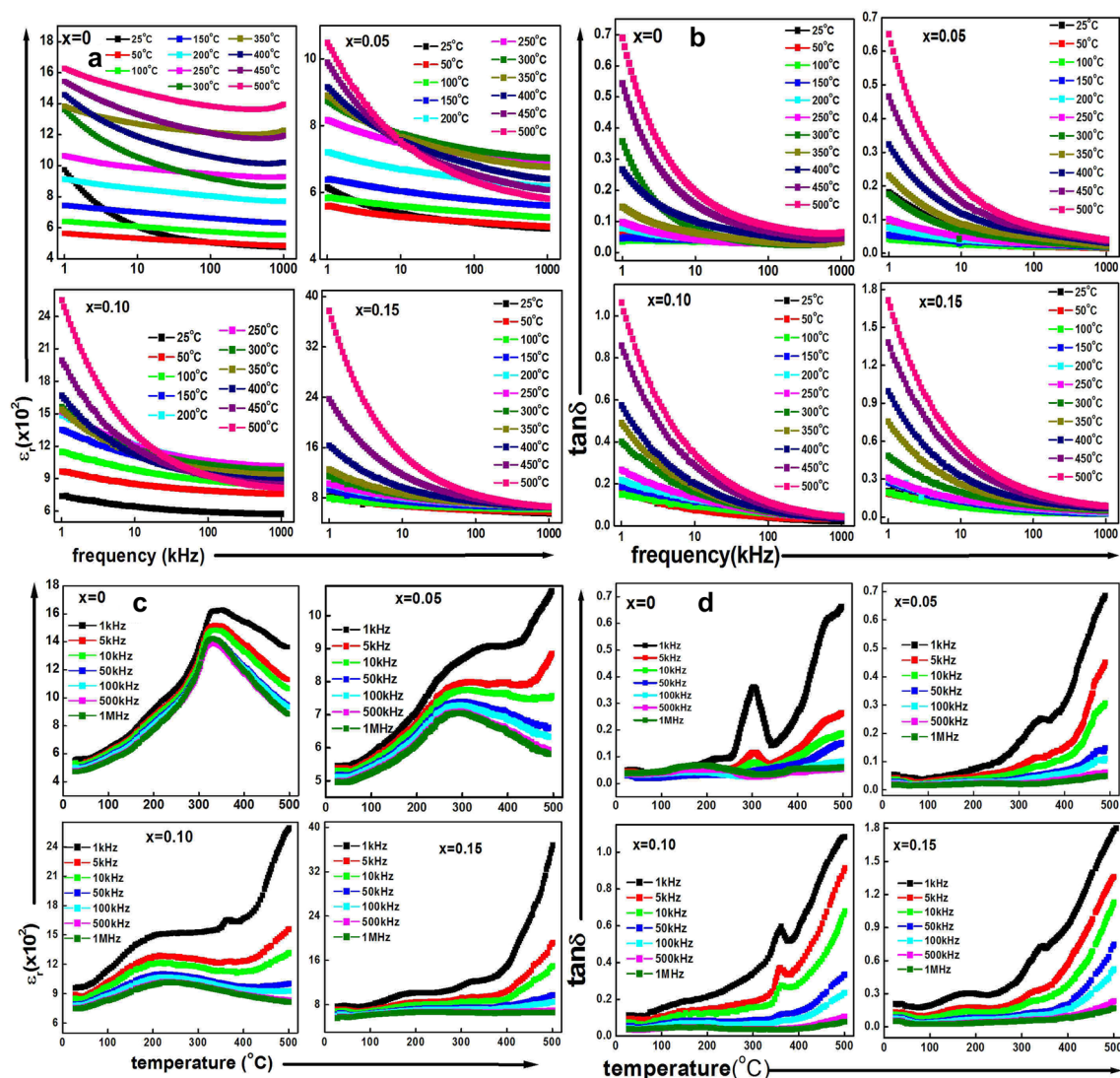


Figure 3: Effect of frequency on (a) dielectric constant and (b) loss tangent at various temperatures (25 °C to 500 °C); and effect of temperature on (c) dielectric constant and (d) loss tangent at various frequencies (1 kHz to 1 MHz) of (1–2x) BNT + x SSn + x SSe compounds with different concentrations.

5%, 10%, 15%) in BNT over a broad temperature (25–500 °C) and frequency (1 kHz to 1 MHz) ranges. It is observed that the value of the relative permittivity reduces with the increase in frequency, and reaches a fixed point at high frequencies. This decreasing trend of the dielectric parameters (ϵ_r and $\tan\delta$) resembles the nature of the polar dielectric materials [35]. For all temperatures and concentrations of the materials, the saturated value of the relative permittivity is achieved at high frequencies (> 1 MHz) (beyond the experimental limit). In the low-frequency region, the various kinds of polarization processes are observed, and the net polarization is thus defined as the sum of all four types of polarization. Hence, ϵ_r shows the maximum value at the low frequencies and then decreases as some polarizations diminish, and finally vanish entirely after a certain frequency limit except for electronic polarization. The

relation between the dielectric constant and the atomic polarizability is well described by the Clausius–Mossotti relation [36]. It is clearly visible that at low frequencies as well as high temperatures, the value of ϵ_r reduces quickly, whereas, in high frequencies, the decreasing rate becomes slower. This may be elucidated by the Maxwell–Wagner theory of Koop’s double-layered model. It is because of the existence of conducting grain (dominating at high frequencies) and poorly conducting grain boundaries (dominating at low frequencies) [37]. On the application of an external electric field, there is an accumulation of charge carriers observed at the grain boundary. With the rise in frequency, the direction of the motion of the charge carriers suddenly changes, and this obstructs the movement of charge carriers within the specimen. As a result, the gathering of the charge carriers gets reduced at the grain boundary, and then the

value of ϵ_r decreases. The reduction of the relative permittivity with the rise in frequency is also caused by the fact that the electron hopping between Ti^{4+} and Ti^{3+} is unable to follow the alternating electric field in the high-frequency region. Hence the electrons have to go through the grain as well as the grain boundary, but because of the high value of resistance of the grain boundary, the electrons/charge carriers are collected there, and create a large value of space charge polarization. Consequently, the relative permittivity possesses a high value in the low-frequency zone. With the substitution of alkaline earth stannate and alkaline earth selenite (SSn+SSe) to the BNT ceramic, the value of relative permittivity first decreases for $x=0.05$, and then rises for other higher concentrations (i.e., for $x=0.10$, and 0.15). On the other hand, the value of the loss tangent decreases with an increase in frequency, and this type of trend may be specified using the dipole relaxation phenomenon [38]. The space charges are not capable to pursue the high frequency of the applied alternating field and go on relaxation. The sharp increase of loss tangent at the low-frequency side may be because of the thermally activated charge carrier's scattering and the presence of some unknown defects in the materials including oxygen vacancies. In the low-frequency region, a large amount of energy is required for the movement of the ions as the grain boundary contains a high value of resistance, hence the dielectric loss shows maximum value in this region, but the reverse situation occurs in the high frequency region.

With the addition of SSn-SSe to BNT, the value of dielectric loss first reduces for $x=0.05$ and then rises for other higher concentrations (i.e., for $x=0.10$, and 0.15). The values of dielectric constant at 1 kHz and 500 °C are found to be 1636, 1083, 2607, and 3803 for $x=0, 0.05, 0.10, 0.15$ respectively. Similarly, the loss tangent values are observed to be 0.69, 0.66, 1.08, and 1.79 for $x=0, 0.05, 0.10, 0.15$, respectively.

Effect of temperature on dielectric parameters

Figure 3(c), (d) represents the temperature dependence of dielectric parameters (dielectric constant as well as loss tangent) of $(1-2x)$ BNT + x SSn + x SSe with different concentrations at selected frequency (1 kHz to 1 MHz). In this figure, BNT and its modified compounds contain two dielectric anomalies (peaks) in the graph. These anomalies correspond to the two values of temperatures, identified as the depolarization temperature (T_d) and maximum temperature (T_m) respectively. In normal ferroelectric materials, these two peaks coincide with one another and are usually called the Curie temperature (T_c). At the Curie temperature, the phase transition of the materials goes from the ferroelectric to the paraelectric phase; i.e., above T_c , the paraelectric phase, and below T_c ferroelectric phase [39]. However, in the BNT+SSn+SSe system, this situation does not occur. The depolarization temperature (T_d) corresponds to the ferroelectric

to the anti-ferroelectric transition, whereas at maximum temperature (T_m) the phase transition from the anti-ferroelectric to the para-electric state takes place [7]. T_d is smaller than that of T_m , and can be evaluated from the first peak of $\tan \delta$ vs temperature plot. BNT has a complex phase structure; the rhombohedral structure of the BNT compound is transferred to the tetragonal structure at about 260 °C and from the tetragonal to the cubic structure at around 540 °C [40]. In the present study, the first peak is observed at around 200 °C (known as the T_d) and the second one is observed between 320 and 350 °C (called as the T_m). In the figure, it is clearly seen that with an increase in temperature, both ϵ_r and $\tan \delta$ increase. This nature of the variation of dielectric parameters was explained by Schmidt et al. [41]. According to them, this is due to the super paraelectric cluster polarization and the Maxwell–Wagner effect. In the present work, with the addition of SSn+SSe to BNT, the dielectric constant first decreases for $x=0.05$, and then rises for $x=0.10$ and 0.15 . The dielectric loss varies in a similar way as that of the dielectric constant. The value of loss tangent remains constant up to 100 °C, and then increases with further increase in temperature. A small peak is observed between 100 and 200 °C, and a prominent peak is observed at around 350 °C for all compositions of the compounds. These two peaks also correspond to the peaks observed in the dielectric constant plot. The increase of dielectric loss with an increase in temperature suggests the existence of the thermally activated conduction process in the studied materials. Again, it is observed that at low frequencies and high temperatures, the dielectric loss increases quickly because of the free movement of space charges in this region. It is now clear that the materials possess a very small value of $\tan \delta$ which makes the materials useful for different electronic devices.

Impedance spectroscopy

Impedance spectroscopy is an effective, powerful as well as unique technique to study the electrical properties of the polycrystalline, ionic, and dielectric materials. This is a non-destructive method that correlates the micro-structure (containing grain as well as grain boundary) of the compounds with the electrical properties. This process is generally used to distinguish the effect of grain, grain boundary as well as electrode interface effect on the electrical impedance of the substances. It takes into account the movement of mobile charges in the bulk and interfacial zones [42]. The external electric signal is applied across the sintered pellets, and the output impedance data are expressed as a function of temperature and frequency. The complex impedance of the materials consists of both real (Z') as well as imaginary (Z'') components, that are expressed through the following relations,

$$Z^* = Z' + jZ'' \quad (4)$$

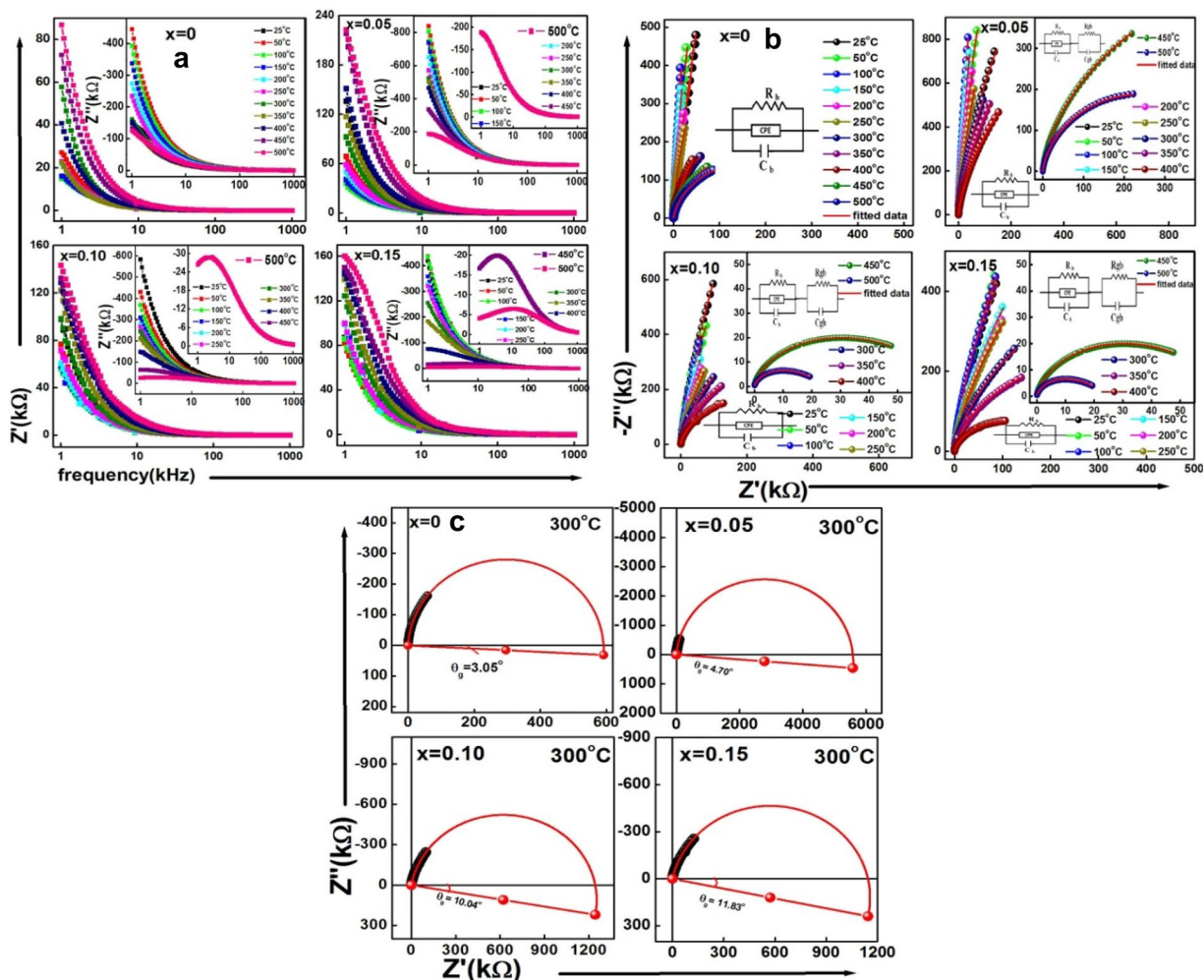


Figure 4: (a) Variation of Z' and Z'' with frequency; (b) Nyquist plots at various temperatures out of 25 to 500 °C; (c) Depressed semicircles at 300 °C with depression angle of $(1-2x)$ BNT + x SSn + x SSe compounds with various concentrations.

$$\text{Here, } Z' = \frac{R}{1 + (\omega\tau)^2} \text{ and} \quad (5)$$

$$Z'' = \frac{\omega R\tau}{1 + (\omega\tau)^2} \quad (6)$$

Here τ stands for relaxation time and is defined as the product of R and C .

Effect of frequency on Z' and Z''

Figure 4(a) represents the frequency variation of Z' and Z'' (inserted) of the studied compounds BNT+SSn+SSe (with $x=0, 0.05, 0.10, 0.15$) at various temperature of (25–500 °C) in a broad frequency range (1 kHz to 1 MHz). In the region of low-frequency, with the increase in temperature, the value of Z' decreases whereas for higher frequencies, the values of Z' merge to a fixed value irrespective of temperature rise. Such type of nature of the plot suggests the liberation of space

charge due to the lowering of the barrier property of the compound with an increase in temperature and this is responsible for the rise in ac conductivity of the compound with frequency [43]. In the present study, Z' value reduces with temperature rise from 25 to 100 °C, and with a further rise in temperature, Z' increases up to 500 °C for all four compositions of the materials. It indicates that in the low-temperature zone, the material possesses the NTCR (negative temperature coefficient of resistance) behavior and in the high-temperature zone, PTCR (positive temperature coefficient of resistance) behavior is observed in the studied compounds. At high frequencies, the space charges have a very small time for relaxation, and thus recombination becomes faster. Therefore, in the high-frequency region, the space charge polarization decreases which gives rise to the overlapping of Z' values. The nature of variation of Z' curves shows the presence of a single relaxation mechanism, which indicates the enhancement of ac conductivity with a rise in both temperature and frequency.

In the Z'' versus frequency graphs, the Z'' follows a similar trend. The value of imaginary components of complex impedance reduces with an increase in both temperature and frequency and combines to a constant value after 100 kHz indicating the space charge accumulation in the compounds. The Z'' graph of the compound shows a characteristic peak corresponding to a certain value of frequency at high temperatures, known as a relaxation peak. In the present work, within the experimental range of frequency as well as temperature, the peak is absent in the parent compound suggesting the absence of dissipation of current, whereas, it is exhibited in the other three compositions. With an increase in the added amounts of SSn and SSE, the peak becomes more prominent (i.e., it is clearly visible for $x=0.15$ at 450 °C and 500 °C). This is because of the fact that the peak has a tendency to appear at low frequency and high temperature. Hence, in the parent compound (BNT), the peak may present at a frequency lower than 1 kHz. The existence of the peak (originated from the dipolar polarization) represents the relaxation mechanism present in the compounds [44]. For $x=0.15$ graph, it is clearly observed that the maximum value of Z'' is observed and moves towards the high-frequency zone with the rise in temperature from 450 to 500 °C. It proposes the increase in $\tan \delta$ value with temperature rise. This shift is also accompanied by the reduction of the amplitude. These observations confirm the presence of the relaxation process and indicate the semiconductor behavior of the material [42]. In this plot, a broadening is found in the peak with the rise in temperature, which indicates the temperature dependence of the relaxation phenomenon. The height of the peak varies directly with the bulk/grain resistance (R_b), and is confirmed by Eq. (6) [45].

The relaxation mechanism is because of the occurrence of immobile charge carriers at low temperatures and the defects like oxygen vacancy at high temperatures in dielectric samples [46]

Nyquist plot

Figure 4(b) represents the temperature-dependent complex impedance spectra commonly known as the Nyquist plots of the studied compounds over a wide range of frequencies (1 kHz to 1 MHz) at different compositions. The impedance spectroscopy of the samples is studied with the development of complex semicircles whose pattern varies with temperature. The shape of the semicircular arcs is determined by the conductivity as well as the polarization mechanism present in the compounds. In this figure, it is observed that except for the parent compound, for other composition of the materials, the impedance curves are fitted by a single semicircle in the low-temperature region (25–400 °C), and by two semicircles at high temperatures (450 °C and 500 °C) but in the parent

compound, all the curves are fitted by a single semicircle. The degree of intercept of the semicircles and the number of semicircles give evidence regarding the electrical process that exists in the materials. It is observed in the graphs that, initially, the curves are almost straight lines, and with the rise in temperature, the lines are bent to form semicircular arcs. In other words, the radius of the semicircular arcs is maximum at low temperatures. With the rise in temperature, the radius of the curve declines and approaches the real Z -axis. This type of result reveals that the conduction mechanism is thermally activated and proves the semiconductor behavior of the material [42]. The relationship between the semicircles and the microstructure of the compounds is explained by the equivalent circuit elements using Z-SimpWin software. The first semicircle represents the influence of the grain effect and the second one is for the grain boundary effect on the resistive and capacitive properties. In this figure, for $x=0$, all curves are fitted by the corresponding electrical circuit of RQC where resistor and capacitor are connected in parallel combination with Q , the constant phase element (CPE) between them. Similarly, for other compositions of the materials, all impedance curves from room temperature to 400 °C are fitted through the RQC circuit, and other curves are modeled by the RQC-RC circuit where R and C are connected in parallel. In the plot, the solid symbol signifies the experimental data and the red line represents the fitted data with a very good matching is observed between them (with a small value of chi-squares). The values of resistance and capacitance and constant phase element of grain (i.e., R_g , C_g , and Q) and grain boundary (i.e., R_{gb} , and C_{gb}) are calculated from the fitted data and are compared in Table 2. The observed semicircular arcs have their center below the real Z -axis suggesting the existence of the non-Debye type relaxation process in the compounds [47]. For the ideal Debye model, the semicircle with its center lying on the real Z -axis is observed. The CPE presents in the equivalent circuit elements also confirms the deviation from the ideal Debye type model in the studied materials. With the increase in temperature, the area of the semicircular arc decreases which proposes the relaxation mechanism is temperature-dependent. For better investigation of the non-Debye type relaxation process, the depressed semicircles are drawn at 300 °C for all compounds. The different values of the depression angles 3.05°, 4.70°, 10.04°, and 11.83° are observed for $x=0, 0.05, 0.10,$ and 0.15 , respectively confirming the non-Debye type of relaxation mechanism in the material in the experimental range of temperature as well as frequency.

Conductivity study

In the case of dielectric and ferroelectric materials, studies of electrical conductivity connected with the physical properties,

TABLE 2: Resistance, CPE (Q), and capacitance of grain and grain boundary of $(1-2x)$ BNT + x SSn + x SSe with various concentrations at some selected temperatures (25 °C to 500 °C).

Composition	Temp (°C)	Model	$R_b(\Omega)$	CPE	$C_b(F)$	$R_{gb}(\Omega)$	$C_{gb}(F)$
x=0	25	(RQC)	9.46×10^{06}	5.13×10^{-10}	2.90×10^{-10}		
	50	(RQC)	9.26×10^{05}	3.45×10^{-10}	9.05×10^{-11}		
	100	(RQC)	8.81×10^{05}	4.98×10^{-10}	6.07×10^{-14}		
	150	(RQC)	2.65×10^{07}	5.88×10^{-10}	1.50×10^{-16}		
	200	(RQC)	6.10×10^{07}	7.19×10^{-10}	2.11×10^{-14}		
	250	(RQC)	7.14×10^{07}	8.00×10^{-10}	3.98×10^{-14}		
	300	(RQC)	7.28×10^{07}	1.58×10^{-10}	7.26×10^{-10}		
	350	(RQC)	8.66×10^{07}	2.34×10^{-10}	8.13×10^{-10}		
	400	(RQC)	1.19×10^{08}	3.24×10^{-09}	6.80×10^{-10}		
	450	(RQC)	2.70×10^{08}	4.86×10^{-09}	5.85×10^{-10}		
x=0.05	25	(RQC)	9.70×10^{07}	7.35×10^{-10}	1.60×10^{-10}		
	50	(RQC)	8.05×10^{07}	1.46×10^{-10}	1.60×10^{-10}		
	100	(RQC)	5.99×10^{07}	9.84×10^{-10}	1.52×10^{-10}		
	150	(RQC)	9.92×10^{07}	1.74×10^{-10}	1.74×10^{-10}		
	200	(RQC)	1.42×10^{08}	2.06×10^{-10}	1.89×10^{-10}		
	250	(RQC)	2.77×10^{08}	3.93×10^{-10}	2.18×10^{-10}		
	300	(RQC)	4.81×10^{08}	7.05×10^{-10}	2.24×10^{-10}		
	350	(RQC)	6.96×10^{08}	1.03×10^{-09}	2.15×10^{-10}		
	400	(RQC)	8.18×10^{08}	1.43×10^{-09}	2.01×10^{-10}		
	450	(RQC)(RC)	8.55×10^{08}	5.00×10^{-09}	2.75×10^{-10}	7.41×10^{08}	5.84×10^{-10}
500	(RQC)(RC)	9.22×10^{08}	5.59×10^{-09}	1.83×10^{-10}	7.99×10^{08}	2.02×10^{-10}	
x=0.10	25	(RQC)	2.28×10^{07}	1.17×10^{-09}	1.95×10^{-10}		
	50	(RQC)	9.92×10^{06}	1.43×10^{-09}	2.66×10^{-10}		
	100	(RQC)	5.39×10^{06}	1.19×10^{-09}	2.73×10^{-10}		
	150	(RQC)	1.67×10^{07}	2.42×10^{-09}	3.02×10^{-10}		
	200	(RQC)	3.11×10^{07}	2.91×10^{-09}	3.28×10^{-10}		
	250	(RQC)	4.34×10^{07}	6.36×10^{-09}	3.52×10^{-10}		
	300	(RQC)	5.28×10^{07}	8.33×10^{-09}	3.42×10^{-10}		
	350	(RQC)	5.42×10^{07}	1.44×10^{-08}	3.29×10^{-10}		
	400	(RQC)	6.54×10^{07}	2.70×10^{-08}	3.11×10^{-10}		
	450	(RQC)(RC)	7.24×10^{07}	4.21×10^{-08}	2.93×10^{-10}	2.63×10^{07}	9.93×10^{-06}
500	(RQC)(RC)	9.07×10^{07}	8.81×10^{-08}	2.78×10^{-10}	4.98×10^{07}	1.53×10^{-07}	
x=0.15	25	(RQC)	6.83×10^{06}	1.09×10^{-09}	2.09×10^{-10}		
	50	(RQC)	1.82×10^{06}	1.61×10^{-09}	2.35×10^{-10}		
	100	(RQC)	1.05×10^{06}	2.47×10^{-09}	2.64×10^{-10}		
	150	(RQC)	4.01×10^{06}	5.15×10^{-09}	2.73×10^{-10}		
	200	(RQC)	7.93×10^{06}	4.02×10^{-09}	2.75×10^{-10}		
	250	(RQC)	9.34×10^{06}	3.07×10^{-09}	2.71×10^{-10}		
	300	(RQC)	2.35×10^{07}	4.80×10^{-09}	2.65×10^{-10}		
	350	(RQC)	4.80×10^{07}	8.02×10^{-09}	2.63×10^{-10}		
	400	(RQC)	5.47×10^{07}	2.46×10^{-08}	2.64×10^{-10}		
	450	(RQC)(RC)	6.08×10^{07}	7.42×10^{-08}	2.63×10^{-10}	1.17×10^{07}	1.37×10^{-10}
500	(RQC)(RC)	6.51×10^{07}	2.35×10^{-07}	2.59×10^{-10}	1.26×10^{07}	4.20×10^{-08}	

such as dielectric, impedance, and modulus are associated with their response to the applied electrical signal. The electrical conduction mechanism provides essential information regarding the electrical transport process of the ions/charge carriers (including electrons/holes) present inside the materials. Depending on the nature of the charge carriers, any material can be classified as a conductor, semiconductor or insulator. In

the semiconducting region, the variable range hopping (VRH) model and small polaron hopping (SPH) model were used to explain the conduction, however, in the metallic region, the transport is governed by the scattering mechanisms like as electron–electron, electron–phonon scattering [48]. Total electrical conductivity consists of two components; (i)

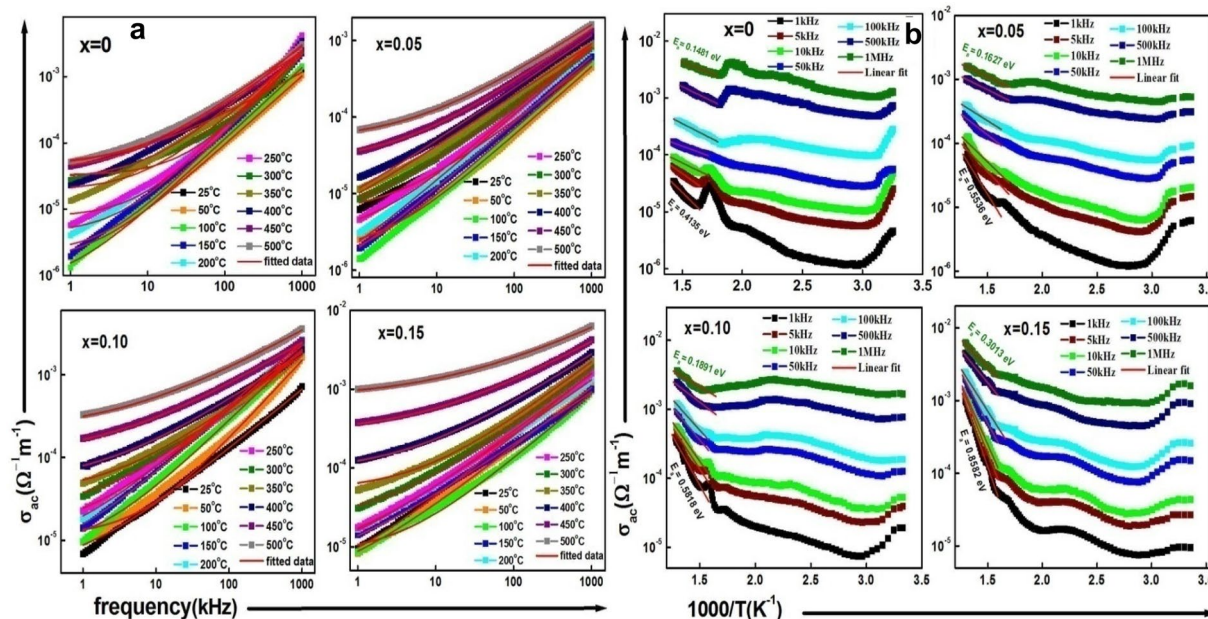


Figure 5: Variation of ac conductivity with (a) frequency at different temperature (25–500 °C) and (b) inverse of absolute temperature at different frequency (1 kHz to 1 MHz) of (1–2x) BNT + x SSn + x SSe compounds with various concentrations.

frequency-independent dc conductivity (σ_{dc}) and (ii) frequency-dependent ac conductivity (σ_{ac}), and represented by the following equation,

$$\sigma_T = \sigma_{ac} + \sigma_{dc} \quad (7)$$

Among these two components, ac conductivity plays a vital role in the electrical conductivity study of the materials which can be expressed in terms of dielectric parameters by using the empirical formula,

$$\sigma_{ac} = \omega \epsilon_0 \epsilon_r \tan \delta \quad (8)$$

Here each term possesses the usual meaning.

Effect of frequency on ac conductivity

Figure 5(a) represents the frequency variation of σ_{ac} of the prepared compounds for all compositions at different temperatures in the range of 25 to 500 °C. In the low-temperature region, with an increase in frequency, the value of ac conductivity increases sharply. But with the rise in temperature, the increasing rate of conductivity becomes slower. After a certain temperature, the ac conductivity curves become independent of frequency. At high temperatures in the low-frequency site, the graph displays the frequency-independent (plateau) behaviors, and thus represents the dc conductivity. On the other hand, the frequency dispersion part corresponds to the high-frequency side representing the σ_{ac} . In the graph, for the high value of the substituted compositions (i.e., for $x=0.10$, and 0.15), the plateau region is more prominent than that of other concentrations ($x=0$, and 0.05). The enhancement of ac conductivity

with frequency as well as temperature is specified by the cation disordering between the existing space charges and the surroundings. The frequency-dependent curves of the ac conductivity are fitted non-linearly by Jonscher’s universal power-law according to the following equation [49, 50],

$$\sigma_{ac} = \sigma_{dc} + A\omega^n \quad (9)$$

Here σ_{dc} is the dc conductivity, $\omega = 2\pi f$ is the angular frequency, A represents a constant known as the pre-exponential factor and n represents the frequency exponent has been found to be material dependent with the value of $0 < n < 1$; and both A and n are temperature dependent. ‘A’ defines the polarizability strength, and ‘n’ determines the degree of interaction between the mobile charge carrier and the lattices surrounding them. The value of the dc conductivity, A, and n of the materials at different concentrations (x) with the obtained values of error during fitting are given in Table 3. It is noticed that the value of n lies between 0 and 1. According to Jonscher, the frequency variation of ac conductivity originates because of the relaxation mechanism, produced by the mobile ions/charge carriers [51]. The switching of frequency-dependent σ_{ac} from the frequency-independent σ_{dc} is because of the relaxation process and the transformation from hopping at a long range to the motion of ions/electrons at a short-range [52].

Effect of temperature on ac conductivity

Figure 5(b) shows the variation of σ_{ac} with the inverse absolute temperature of the compounds BNT+SSn+SSe for various

TABLE 3: Values of σ_{dc} , A and n of (1–2x) BNT + x SSn + x SSe compounds with various concentrations with the error.

Compo- sition	Temper- ature	σ_{dc}	A	n	Error (κ^2)
x=0	25	4.213×10^{-05}	1.179×10^{-07}	0.663	4.607×10^{-10}
	50	1.630×10^{-06}	6.101×10^{-10}	0.937	2.890×10^{-11}
	100	7.311×10^{-07}	4.758×10^{-10}	0.976	9.396×10^{-11}
	150	2.253×10^{-06}	2.172×10^{-10}	0.665	3.711×10^{-10}
	200	4.454×10^{-06}	2.939×10^{-10}	0.854	4.871×10^{-10}
	250	7.786×10^{-06}	2.289×10^{-10}	0.773	3.721×10^{-10}
	300	3.528×10^{-05}	2.068×10^{-10}	0.870	2.116×10^{-09}
	350	2.615×10^{-05}	1.651×10^{-09}	0.926	3.340×10^{-09}
	400	3.125×10^{-05}	2.920×10^{-09}	0.802	6.182×10^{-09}
	450	4.587×10^{-05}	2.828×10^{-08}	0.821	1.734×10^{-09}
x=0.05	500	5.721×10^{-05}	1.950×10^{-08}	0.859	2.007×10^{-09}
	25	5.399×10^{-06}	9.291×10^{-09}	0.792	2.190×10^{-12}
	50	1.650×10^{-06}	1.823×10^{-09}	0.899	1.657×10^{-12}
	100	9.531×10^{-07}	2.507×10^{-09}	0.887	8.533×10^{-12}
	150	4.085×10^{-07}	4.194×10^{-09}	0.860	3.327×10^{-12}
	200	3.922×10^{-07}	5.030×10^{-09}	0.866	2.799×10^{-12}
	250	2.662×10^{-06}	4.548×10^{-09}	0.883	1.231×10^{-11}
	300	4.624×10^{-06}	4.624×10^{-06}	0.763	1.633×10^{-11}
	350	1.610×10^{-06}	8.312×10^{-08}	0.672	2.884×10^{-11}
	400	2.016×10^{-06}	8.299×10^{-08}	0.691	3.790×10^{-11}
x=0.10	450	3.638×10^{-05}	8.638×10^{-08}	0.700	1.969×10^{-11}
	500	5.028×10^{-05}	1.909×10^{-07}	0.651	4.012×10^{-11}
	25	4.164×10^{-06}	3.162×10^{-08}	0.720	6.882×10^{-11}
	50	1.005×10^{-05}	2.575×10^{-09}	0.960	6.169×10^{-10}
	100	7.592×10^{-06}	1.439×10^{-08}	0.856	6.786×10^{-10}
	150	5.402×10^{-06}	4.695×10^{-08}	0.781	1.022×10^{-09}
	200	7.606×10^{-06}	5.895×10^{-08}	0.770	1.089×10^{-09}
	250	1.505×10^{-05}	7.207×10^{-08}	0.740	1.183×10^{-09}
	300	2.375×10^{-05}	1.045×10^{-07}	0.708	1.553×10^{-09}
	350	4.255×10^{-05}	1.861×10^{-07}	0.660	9.137×10^{-10}
x=0.15	400	5.628×10^{-05}	5.076×10^{-07}	0.592	7.471×10^{-10}
	450	1.115×10^{-05}	1.491×10^{-06}	0.533	6.232×10^{-10}
	500	2.105×10^{-05}	3.366×10^{-06}	0.497	9.774×10^{-10}
	25	3.115×10^{-06}	2.772×10^{-08}	0.793	1.528×10^{-11}
	50	3.157×10^{-06}	3.060×10^{-08}	0.755	1.036×10^{-10}
	100	7.961×10^{-06}	8.534×10^{-09}	0.834	1.531×10^{-10}
	150	4.833×10^{-06}	8.977×10^{-08}	0.668	2.085×10^{-10}
	200	6.475×10^{-06}	8.907×10^{-08}	0.694	6.182×10^{-11}
	250	6.799×10^{-06}	6.282×10^{-08}	0.731	7.125×10^{-11}
	300	2.891×10^{-05}	7.963×10^{-08}	0.729	1.236×10^{-10}
350	5.790×10^{-05}	7.220×10^{-08}	0.746	1.499×10^{-10}	
400	9.025×10^{-05}	4.018×10^{-07}	0.637	7.068×10^{-10}	
450	2.834×10^{-05}	1.793×10^{-06}	0.553	1.512×10^{-09}	
500	7.871×10^{-05}	6.945×10^{-06}	0.480	2.896×10^{-09}	

compositions at some selected frequency in the range of 1 kHz to 1 MHz. The value of ac conductivity changes very slowly in the low-temperature zone and very quickly in the high-temperature region. The activation energy of the thermally activated process can be evaluated by using the formula,

$$\sigma = \sigma_0 \exp\left(\frac{-E_a}{K_B T}\right) \quad (10)$$

where σ_0 stands for the pre-exponential factor and K_B represents the Boltzmann constant. The equation is valid for the excitation of free electrons from the Fermi level to the highest density of states. The values of the activation energy are evaluated from the slopes of the linear fitting lines in the high-frequency region and tabulated in Table 4 with the corresponding chi-square value. With the rise in frequency, the value of activation energy decreases for all x values. The different values of E_a suggest the presence of different conduction processes in the compounds. The calculated value of E_a is the summation of the activation energies of the charge carriers along with the free energy of the carrier hopping. With the rise in frequency, the probability of hopping of the charge carriers increases, and this reduces the values of E_a with frequency rise.

In the high-temperature region, the high values of electrical conductivity are due to the oxygen vacancies produced during the high-temperature sintering process [53]. The steepness of the slopes in the low-frequency region for all compositions (x) shows the dominating behavior of dc conductivity. It is observed that the values of activation energy of the materials increase with the increase of the substituted amount (x) for all frequencies.

J–E characteristics and polarization study

The electric field (E) variation of current density J (i.e., J–E characteristics) of the prepared compounds BNT + SSn + SSe for all concentrations at various temperatures in the range of 25–500 °C are shown in Fig. 6(a)–(c). Figure 6(a) displays the current density vs. electric field of the materials in both positive and negative polarities starting from – 400 V/cm to 400 V/cm through the origin. The value of J rises smoothly up to 50 V/cm for all compositions and after this, the increasing rate becomes slower. This figure is symmetric on both sides of the origin. It is observed from the plot that with the rise in temperature the values of leakage current density of the material for all compositions increase. With the rise in the doping percentage, the value of current density decreases. The value of current density at 25 °C is found to be 1.758×10^{-07} A/cm², 1.976×10^{-07} A/cm², 1.165×10^{-07} A/cm², and 1.309×10^{-08} A/cm² for x=0, 0.05, 0.10, 0.15, respectively. The small value of leakage current makes the materials useful for the fabrication of possible electronic devices.

Figure 6(b) depicts the log J vs. log E plot for all compositions in the experimental range of temperature. Here the log J curves are fitted linearly with the slope $m \approx 1$ in the both high and low-electric field regions. This signifies that throughout the field, the materials show Ohmic conduction. In other words, the charge transport mechanism is predominated by Ohmic conduction in accordance with the following equation,

$$J_{\text{ohm}} = q\mu nE \quad (11)$$

where μ is the charge carrier mobility, n represents the electron number density, and E is the electric field strength [54].

In some cases, it is found that in the high-voltage regions, the value of leakage current density increases steeply with the slope closer to 2 (i.e., $m \approx 2$), and this is because of the excess in the accumulation of space charges. Such a type of transportation mechanism, known as the space charge limited current (SCLC) conduction, is absent in the studied materials. The values of the slope of the linear fit current density curves with the corresponding values of error are tabulated in Table 2 in the supplementary material file.

Figure 6(c) represents the variation of $\log J$ with $E^{1/2}$ commonly known as the Schottky emission (SE) plot for all temperatures. The Schottky emission/thermionic emission is well explained by the following relation,

$$J = A^* T^2 \exp \left[\frac{-q(\phi_B - \sqrt{qE/4\pi\epsilon_r\epsilon_0})}{k_B T} \right] \quad (12)$$

where A^* stands, for the Richardson constant, E signifies the electric field across the material, and ϕ_B represents the barrier height [55, 56].

The equation signifies that $\log J$ varies linearly with $E^{1/2}$ and the slope of the linear fitting line provides the dynamic dielectric constant. But, in the present study, the $\log J$ curves are not linear and suggest the absence of SE materials in the said experimental range.

Figure 6(d) reveals the nonlinear relationship between the electric polarization (P) and applied electric field (E) of the synthesized un-poled pellets of different compositions. The P - E hysteresis loop of the materials (taken at room temperature) with a frequency of 50 Hz signifies the ferroelectric nature of the sample. Because of the experimental limitation, a sufficiently high electric field could not be applied to get saturated symmetric loops. The electrode sintered pellets of different area and thickness for various concentrations such as (1.10 cm² and 0.23 cm), (0.98 cm² and 0.25 cm), (0.95 cm² and 0.2,3 cm), and (1.12 cm² and 0.22 cm) for 0, 5%, 10%, and 15% respectively were taken for the measurements. The obtain values of remnant polarization ($2P_r$) and coercive field (E_c) of the compounds are found to be (0.201 $\mu\text{C}/\text{cm}^2$ and 1.629 kV/cm), (0.254 $\mu\text{C}/\text{cm}^2$ and 2.130 kV/cm), (0.450 $\mu\text{C}/\text{cm}^2$ and 2.105 kV/cm), (0.633 $\mu\text{C}/\text{cm}^2$ and 1.828 kV/cm) for $x=0, 0.05, 0.1, 0.15$, respectively. It is clear that with the rise in substitution concentration the $2P_r$ value of the parent compounds increases successfully.

Conclusion

BNT + SSn + SSe polycrystalline compound with different compositions has been prepared through the conventional mixed oxide reaction method. The room temperature XRD pattern of

the calcinated powder samples has been considered from 20° to 80° of Bragg diffraction angle, proposing the development of a new perovskite single-phase compound without any impurity phases. The material crystallizes in a rhombohedral crystal system with cell parameters $a=5.4760 \text{ \AA}$ and $c=6.7780 \text{ \AA}$ according to the JCPDS database of bismuth sodium titanate. With the substitution of the SSn-SSe to the BNT compound, the position of the characteristic peaks moves towards the lower diffraction angle because of the higher ionic radii of the substituted compounds in comparison to the pure sample. The crystallite size of the compounds is evaluated using the W-H plot and found to be 57 nm, 65 nm, 67 nm, and 70 nm for $x=0, 0.05, 0.10$, and 0.15 , respectively. The microstructure of the gold-coated pellets displays the homogeneous distribution of grains, separated by the grain boundary and the size of grains varies from 0.28 to 1.61 μm . The dielectric property and the polarization processes of the material are described by the Clausius-Mossotti relation. The dielectric graph contains two dielectric anomalies corresponding to T_d (ferroelectric to anti-ferroelectric transition) and T_m (anti-ferroelectric to paraelectric transition) observed around 200 and 350 °C, respectively. The high value of the relative permittivity and small values of dielectric loss makes the compound preferable for device application. In the impedance spectroscopy, the material exhibit both NTCR (at a lower temperature) as well as PTCR (at a higher temperature) behaviors, and the contribution of grain and grain boundary effects are explained by the Nyquist plot. The depressed semicircles with certain values of the depression angles are displayed at 300 °C indicating the non-Debye type relaxation mechanism exists in the compound. The ac-conductivity curves are fitted through Jonscher's universal power-law model and the activation energy at a higher temperature for all frequencies is evaluated using the Arrhenius equation. With the increase in frequency, the decrease in E_a suggests the rise in the probability of the hopping of the charge carriers. The J - E characteristics of the compound show a very small amount of leakage current density of the order of $10^{-7} \text{ A}/\text{cm}^2$ at room temperature and with temperature rise, this value increases up to $10^{-4} \text{ A}/\text{cm}^2$. The slope of the $\log J$ vs. $\log E$ is observed nearly equal to 1 indicating the conduction process is of Ohmic type. The room temperature polarization vs. electric field hysteresis loop suggests the ferroelectric nature of the studied material. With the substitution of SSn-SSe the $2P_r$ values of the compound gradually increase.

Synthesis and characterization techniques

Two crystal systems (SrSnO₃+SrSeO₃) modified (Bi_{0.5}Na_{0.5})TiO₃ solid solutions of standard chemical compositions (1-2x)(Bi_{0.5}Na_{0.5})TiO₃ + x(SrSnO₃) + x(SrSeO₃) (referred as BNT + SSn + SSe) with various compositions (i.e., $x=0, 0.05, 0.10$ and 0.15) have been synthesized through a mixed

TABLE 4: Comparison of E_a (eV) of $(1-2x)$ BNT + x SSn + x SSe with various concentrations at different frequencies.

Frequency (kHz)	Activation energy (E_a)							
	Composition (x) and error (χ^2)							
	$x=0$	(χ^2)	$x=0.05$	(χ^2)	$x=0.10$	(χ^2)	$x=0.15$	(χ^2)
1	0.413	0.051	0.553	0.090	0.581	0.010	0.858	0.069
5	0.302	0.021	0.362	0.060	0.488	0.011	0.556	0.086
10	0.252	0.014	0.331	0.057	0.457	0.093	0.680	0.073
50	0.235	0.017	0.265	0.043	0.380	0.074	0.560	0.063
100	0.221	0.009	0.225	0.029	0.297	0.064	0.470	0.063
500	0.200	0.001	0.210	0.008	0.224	0.058	0.366	0.048
1000	0.148	0.012	0.162	0.010	0.189	0.054	0.301	0.040

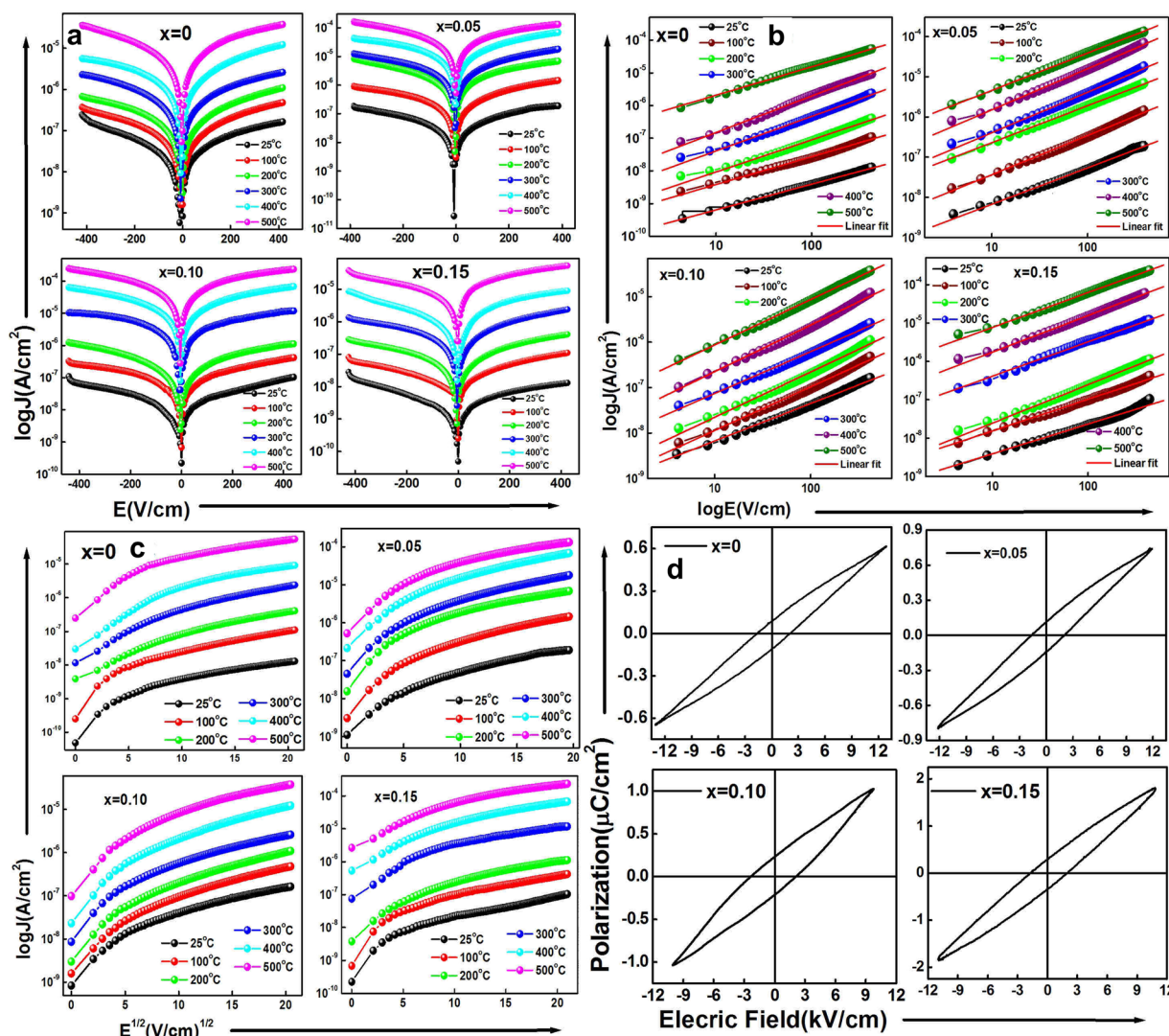


Figure 6: Variation of (a) $\log J$ with E ; (b) $\log J$ with $\log E$; (c) $\log J$ with $E^{1/2}$ at different temperatures of the range of 25–500 °C; (d) Room temperature hysteresis loop at 50 Hz of $(1-2x)$ BNT + x SSn + x SSe with various concentrations.

oxide solid state reaction route for detailed characterization. The high-purity (AR grade) oxides and carbonates such as bismuth oxide Bi_2O_3 (99.0%), sodium carbonate Na_2CO_3

(> 98%), titanium oxide TiO_2 (99.5%), strontium carbonate SrCO_3 (99.9%), tin oxide SnO_2 (99.9%) (all from M/s Loba Chemie Co Ltd) and selenium oxide SeO_2 (> 98%) from M/S

Merck-Schuchardt were taken in stoichiometric ratio using the digital balance meter (correct up to fourth decimal place). These ingredients were mixed thoroughly in both dry (air) as well as wet (in methanol) medium using agate mortar with a pestle for 5 h to obtain homogeneous mixtures of the constituent oxides and carbonates. The calcination of these mixtures has been carried out using an alumina crucible in the high-temperature muffle furnace at 950 °C for 5 h. The room temperature X-ray diffraction (XRD) pattern/data of the calcined powders were analyzed through diffraction data obtained from Rigaku Ultima IV diffractometer having CuK α radiation with $\lambda = 1.5405 \text{ \AA}$ to give information about the crystal structure and phase formation. After the confirmation of the crystal structure, the calcined powders were mixed with PVA (binder) to prepare cylindrical pellets (1–2 mm thick and 12 mm diameter) using KBr hydraulic press at a pressure of $4 \times 10^5 \text{ N/m}^2$. The prepared green pellets were sintered at 1000 °C in the high-temperature muffle furnace to obtain highly dense and hard pellets. The surface micrograph of the gold-coated sintered pellets was recorded employing a scanning electron microscope (SEM) of Zeiss Supra 40. For the electrical measurements, a compact sintered pellet of each composition was polished with fine sand paper and electrode using silver paint. The dielectric, impedance and conductivity analysis of these pellets were performed by using the phase-sensitive meter (PSM 1735) over a wide frequency (1 kHz to 1 MHz) range at different temperatures (25–500 °C). The ferroelectricity in the prepared pellets was established from the room temperature field-dependent polarization i.e., (P - E) hysteresis loop traced using an M/S Marine India hysteresis loop tracer. The leakage current characteristics along with the conduction mechanism of the synthesized compounds were carried out using a Keithley electrometer (6517B).

Acknowledgments

The authors would like to extend their sincere thanks and gratitude to Mr. Nirakar Prasad Samantray, S'O'A (Deemed to be University), for some experimental help.

Data availability

The authors confirm that the data supporting the findings of this work are available within the article. Raw data that support the findings of the study are available from the corresponding author, upon reasonable request.

Declarations

Conflict of interest The authors declare that there is no conflict of interests regarding the publication of this paper.

Supplementary Information

The online version contains supplementary material available at <https://doi.org/10.1557/s43578-023-01099-2>.

References

1. K. Uchino, *Piezoelectric Actuators and Ultrasonic Motors* (Springer, New York, 1997), p. 61
2. E. Benes, M. Groschl, W. Burger, M. Schmlid, *Sens. Actuator A* **48**, 1–21 (1995)
3. A. Banerjee, S. Bose, *Chem. Mater.* **16**, 5610–5615 (2004)
4. N. Chakrabarti, H.S. Maiti, *Mater. Lett.* **30**, 169–173 (1997)
5. G.A. Smolenskii, V.A. Isupov, A.I. Agranovskaya, N.N. Krainik, *Sov. Phys. Solid State* **2**, 2651–2654 (1961)
6. J.A. Zvirgzds, P.P. Kapostins, J.V. Zvirgzde, T.V. Kruzina, *Ferroelectrics* **40**, 75–77 (1982)
7. C. Zhou, X. Liu, *J. Mater. Sci.* **19**, 29–32 (2008)
8. G.O. Jones, P.A. Thomas, *Acta Crystallogr. Sect. B* **56**, 426–430 (2000)
9. Y. Xie, H. Hao, Z. Huang, S. Zhang, M. Cao, Z. Yao, H. Liu, J. *Alloys Compd* **884**, 161031 (2021)
10. S.H. Wu, P. Chen, J.W. Zhai, B. Shen, P. Li, F. Li, *Ceram. Int.* **44**, 21289–21294 (2018)
11. A. Herabut, A. Safari, *J. Am. Ceram. Soc.* **80**, 2954–2958 (1997)
12. W. Lu, S. Jiang, D. Zhou, S. Gong, *Sens. Actuator A* **80**, 35–37 (2000)
13. W.W. Coffeen, *J. Am. Ceram. Soc.* **36**, 207–214 (1953)
14. W.F. Zhang, J. Tang, J. Ye, *Chem. Phys. Lett.* **418**, 174–178 (2006)
15. C.P. Udawatte, M. Kakihana, M. Yoshimura, *Solid State Ion.* **128**, 217–226 (2000)
16. H. Mizoguchi, H.W. Eng, P.M.W. Ward, *Inorg. Chem.* **43**, 1667–1680 (2004)
17. N. Al-Dahoudi, H. Bisht, C. Gobbert, T. Krajewski, M.A. Aegerter, *Thin Solid Films* **392**, 299–304 (2001)
18. Z. Lu, J. Liu, J. Tang, Y. Li, *Inorg. Chem. Commun.* **7**, 731–733 (2004)
19. T. Truttman, A. Prakash, J. Yue, T.E. Mates, B. Jalan, *Appl. Phys. Lett.* **115**, 152103 (2019)
20. T. Wang, A. Prakash, Y. Dong, T. Truttman, A. Bucsek, R. James, D.D. Fong, J.W. Kim, P.J. Ryan, H. Zhou, T. Biro, B. Jalan, *A.C.S. Appl. Mater. Interfaces* **10**, 43802–43808 (2018)
21. H. Chen, N. Umezawa, *Int. J. Photoenergy* **2014**, 1–3 (2014)
22. M.-L. Liang, Y.-X. Ma, C.-L. Hu, F. Kong, J.-G. Mao, *Dalton Trans.* **47**, 1513–1519 (2018)
23. L.T. Vlaev, M.M. Nikolova, G.G. Gospodinov, *Monatshefte Chem.* **136**, 1553–1566 (2005)
24. M. Wildner, G. Giester, N. Jb, *Miner. Abh* **184**, 29–37 (2007)
25. B. Deb, A. Ghosh, *J. Appl. Phys.* **112**, 024102 (2012)

26. Q. Chen, K. Su, Z. Zhao, Q. Ma, J. Non-Cryst. Solids **498**, 448–454 (2018)
27. A. Bachvarova-Nedelcheva, R. Iordanova, St. Yordanov, Y. Dimitriev, J. Non-Cryst. Solids **355**, 2027–2030 (2009)
28. S. Yue, B. Wan, H. Li, Y. Liu, Q. Zhang, Int. J. Electrochem. Sci. **14**, 2049–2062 (2019)
29. W. Chatta, B. Lagoun, H. Lidjici, A. Chadli, A. Cheriet, H. Farh, H. Khemakhem, K. Salah, Solid State Phenom. **297**, 165–172 (2019)
30. B.B. Arya, R.N.P. Choudhary, J. Mater. Sci. **32**, 11547–11567 (2021)
31. W. Zhang, Q. Feng, E. Hosono, D. Asakura, J. Miyawaki, Y. Harada, ACS Omega **5**, 22800–22807 (2020)
32. S. Ilyas, Heryanto, B. Abdullah, D. Tahir, Nano-Struct. Nano-Objects **20**, 100396 (2019)
33. E. Bouzaiene, J. Dhahri, E.K. Hlil, H.H. Hafedh Alrobei, J. Mater. Sci. **31**, 18186–18197 (2020)
34. M. Faraday, Fourteenth Ser. **128**, 189–199 (1837)
35. J.C. Anderson, *Dielectrics* (Chapman and Hall, London, 1964)
36. C. Kittel, *Introduction to Solid State Physics*, 7th edn. (Wiley, Asia, 1996), pp. 381–392
37. C.G. Koops, Phys. Rev. **83**, 121–124 (1951)
38. S. Nath, S.K. Barik, R.N.P. Choudhary, J. Mater. Sci. Mater. Electron. **27**, 8717–8724 (2016)
39. B.J. Chu, D.R. Chen, G.R. Li, Q.R. Yin, J. Eur. Ceram. Soc. **22**, 2115–2121 (2002)
40. W. Li, H. Zeng, K. Zhao, J. Hao, J. Zhai, Ceram. Int. **40**, 7947–7951 (2014)
41. V.H. Schmidt, C.S. Tu, I.G. Siny, Proc. IEEE Int. Symp. Appl. Ferroelectr. **9**, 45–48 (1994)
42. E. Bouzaiene, C. Rayssi, J. Dhahri, A. Afef, H. Belmabrouk, M.A. Albedah, J. Mater. Sci. **34**, 285 (2023)
43. B.B. Arya, R.N.P. Choudhary, Mater. Sci. Eng. B **290**, 116315 (2023)
44. S. Chatterjee, P.K. Mahapatra, R.N.P. Choudhary, A.K. Thakur, Phys. Stat. Solidi. (a) **201**, 588–595 (2004)
45. A.R.V. Hippel, *Dielectrics and Waves* (Wiley Inc, NY, 1954)
46. A.K. Jonscher, Nature **267**, 673–679 (1977)
47. Z. Raddaoui, R. Brahem, A. Bajahzar, H.M. Albetran, J. Dhahri, H. Belmabrouk, J. Mater. Sci. **32**, 23333–23348 (2021)
48. A. Belkahlia, K. Cherif, H. Belmabrouk, A. Bajahzar, J. Dhahri, E.K. Hlil, Solid State Commun. **294**, 16–22 (2019)
49. A.S. Nowick, B.S. Lim, J. Non-Cryst. Solids **172**, 1389–1394 (1994)
50. H. Jain, C.H. Hsieh, J. Non-Cryst. Solids **172**, 1408–1412 (1994)
51. A.K. Jonscher, J. Mater. Sci. **16**, 2037–2060 (1981)
52. R. Mizaras, M. Takashige, J. Banys, S. Kojima, J. Grigas, S.I. Hamazaki, J. Phys. Soc. Jpn. **66**, 2881–2885 (1997)
53. J. Suchanicz, Mater. Sci. Eng. B **55**, 114–118 (1998)
54. A. Sigov, Yu. Podgorny, K. Vorotilov, A. Vishnevskiy, Phase Transit. **86**, 1141–1151 (2013)
55. F.-C. Chiu, Adv. Mater. Sci. Eng. (2014). <https://doi.org/10.1155/2014/578168>
56. S.T. Chang, J.Y.M. Lee, Appl. Phys. Lett. **80**, 655–657 (2002)

Publisher's Note Springer Nature remains neutral with regard to jurisdictional claims in published maps and institutional affiliations.

Springer Nature or its licensor (e.g. a society or other partner) holds exclusive rights to this article under a publishing agreement with the author(s) or other rightsholder(s); author self-archiving of the accepted manuscript version of this article is solely governed by the terms of such publishing agreement and applicable law.